Journal of Solid State Chemistry 206 (2013) 158–169

Contents lists available at ScienceDirect

Journal of Solid State Chemistry

journal homepage: www.elsevier.com/locate/jssc

A neutron diffraction study and mode analysis of compounds of the system $La_{1-x}Sr_xFeO_{3-x}F_x$ ($x=1$, 0.8, 0.5, 0.2) and an investigation of their magnetic properties

Oliver Clemens [a,*,1], Frank J. Berry [a], Adrian J. Wright [a], Kevin S. Knight [b], J.M. Perez-Mato [c], J.M. Igartua [c], Peter R. Slater [a]

[a] School of Chemistry, The University of Birmingham, Birmingham B15 2TT, United Kingdom
[b] ISIS Facility, Rutherford Appleton Laboratory, Harwell Oxford, Didcot, OX11 0QX, United Kingdom
[c] Departamentos de Física de la Materia Condensada y Física Aplicada II, Facultad de Ciencia y Tecnología, Universidad del País Vasco (UPV/EHU), Apdo. 644, 48080 Bilbao, Spain

ARTICLE INFO

Article history:
Received 2 June 2013
Received in revised form
9 August 2013
Accepted 11 August 2013
Available online 17 August 2013

Keywords:
Neutron diffraction
Antiferromagnetism
Perovskite
Fluorination
Iron

ABSTRACT

We report here a detailed study of the system $La_{1-x}Sr_xFeO_{3-x}F_x$, by neutron powder diffraction- and magnetic-measurements. All the compounds are robust antiferromagnetics with ordering temperatures well above room temperature. Magnetic moments are shown to align parallel to the *c*-axis. FC-ZFC measurements indicate a small canting of the magnetic moments, resulting in a ferromagnetic component with a maximum for $La_{0.5}Sr_{0.5}FeO_{2.5}F_{0.5}$. We show that the system exhibits a composition-driven transition from a phase, for low fluorination levels ($x \leq 0.5$), with *Pnma* symmetry and the usual system of octahedral tiltings, to a phase with space group *Imma* for higher fluorine contents, where a correlated distortion of the oxygen octahedra plays a significant role. The consistency of the structural models, with respect to the expected continuity of the amplitudes of the different distortion modes and the invariance of their internal form, was monitored through the symmetry mode decomposition of the structures.

1. Introduction

A variety of applications have been reported for the perovskite-type compounds $La_{1-x}Sr_xFeO_{3-d}$, ranging from oxygen separation membranes to gas sensors [1–6]. Furthermore, these compounds show interesting magnetic properties, varying from antiferromagnetic G-type ordering in $LaFeO_3$ [7,8] to antiferromagnetic ordering in rhombohedral $La_{1/3}Sr_{2/3}FeO_3$, in which ferromagnetic interactions between the magnetic moments on Fe^{3+} and Fe^{5+} in neighbouring layers also occur [9].

Low temperature fluorination reactions (see [10–12] for reviews) are powerful methods for the formation of new oxide fluoride compounds from preformed oxides with concomitant changes in transition metal oxidation state. For iron-containing perovskites, polyvinylidenedifluoride, PVDF [13], has been shown to be a powerful agent for the preparation of the iron-containing perovskite oxide fluorides, such as the compounds $SrFeO_2F$ [14,15], $BaFeO_2F$ (cubic [16,17], 6H [18] and 15R [19] polymorphs), $Sr_xBa_{1-x}FeO_2F$ [20], fluorinated $La_{1-x}Sr_xFe_{1-y}Co_yO_{3-d}$ [21,22], fluorinated $SrFe_{1-x}Sn_xO_{3-d}$ [23] and the system $La_{1-x}Sr_xFeO_{3-x}F_x$ [24].

In these materials the magnetic properties of perovskite-related compounds are influenced by the exchange of O^{2-} for F^- which reduces the average iron oxidation state. Thus, for example, 6H–$BaFeO_{3-d}$ shows antiferromagnetic ordering below 170 K [25–27], whereas the magnetic ordering temperatures of 6H–$BaFeO_2F$ [18] and 6H–$Ba_{0.8}Sr_{0.2}FeO_{3-d}F_{0.2}$HH [28] lie between 600 and 700 K. Although the compounds 15R–$BaFeO_2F$ and 15R–$BaFeO_{2.42}F_{0.2}$ [28] only show a small difference in the average iron oxidation state, the orientation of the spins is different in that the spins align parallel to the *c*-axis for 15R–$BaFeO_{2.42}F_{0.2}$ [28] but are aligned in the a/b-plane for 15R–$BaFeO_2F$ [19].

$La_{1-x}Sr_xFeO_{3-x}F_x$ has been recently reported [24] to undergo a structural distortion from the cubic perovskite structure (*Pm*-3*m*) reported for $SrFeO_2F$ [14,15,20,21] to the orthorhombic perovskite structure (*Pnma*) found for $LaFeO_3$ (e.g. [29]) with decreasing values of the Sr content, *x*. This structural distortion was studied by X-ray powder diffraction and reported to occur in a two-step manner: increasing the metric distortion and shift of mainly the oxygen ions between $x=1$ and $x=0.5$, and a further decrease

* Corresponding author. Fax: +49 6151 16 6335.
E-mail addresses: oliver.clemens@kit.edu, oliver.clemens@nano.tu-darmstadt.de (O. Clemens).
[1] Present address: TU Darmstadt, Joint Research Laboratory Nanomaterials, Petersenstraße 32, 64287 Darmstadt, Germany and KIT, Institut für Nanotechnologie, Hermann-von-Helmholtz-Platz 1, 76344 Eggenstein-Leopoldshafen, Germany

0022-4596/$ - see front matter © 2013 Elsevier Inc. All rights reserved.
http://dx.doi.org/10.1016/j.jssc.2013.08.013

in the metric distortion and additional shift of the La/Sr ions when x is changed from 0.5 to 0. This change was attributed to a lowering of the effective coordination number (ECoN [30]) with the change from Sr^{2+} to La^{3+}.

In this article we report a detailed neutron powder diffraction study of high quality high resolution diffraction data for the compounds $La_{1-x}Sr_xFeO_{3-x}F_x$ ($x=1$, 0.8, 0.5 and 0.2), which has allowed a more detailed understanding of the structural relaxation and has corrected structural descriptions for the compounds with $0.5 < x \leq 1$ as orthorhombic perovskites with space group *Imma*, identifying a distinct new phase within this composition range. Especially for $SrFeO_2F$, which was previously reported to be a simple cubic perovskite by analysis of XRD data [14,15,20,21], it is shown that the structural arrangement of the ions has this lower orthorhombic symmetry, although the cell parameters are pseudocubic. Both the results from the structural study reported in [24] and those reported here have been analyzed and checked in terms of distortion modes with respect to the cubic perovskite. This mode decomposition based in group theory [31] has allowed a quantitative characterization of the peculiarities of the new orthorhombic *Imma* phase found at high fluorination levels (Sr rich samples), in comparison with the *Pnma* phase that is observed at low fluorination levels (La rich samples), and is common to many oxides with distorted perovskite structures. Furthermore, we describe the magnetic properties of the compounds, including the determination of their magnetic structures.

The manuscript is therefore structured as follows: In Section 3.1, we report on the mode analysis which was performed on the structural data received from refinement of XRD data and were reported in [24]. Those investigations motivated us in performing neutron diffraction experiments, and the results of the NPD studies are reported in Section 3.2. At the end of this section we again report on a mode analysis performed on the structures derived from neutron diffraction experiments. Section 4 gives a detailed description of the compound's magnetic properties and structures.

2. Experimental

2.1. Sample preparation

Compounds of composition $La_{1-x}Sr_xFeO_{3-d}$ with a strontium content of $x=1$, 0.8, 0.5, 0.2 and 0 were prepared by a solid state reaction as reported previously [24]. High-purity La_2O_3, $SrCO_3$ and Fe_2O_3 powders were mixed in the appropriate stoichiometric ratio and were thoroughly ground in *n*-pentane. The La_2O_3 powder was first calcined at 1100 °C for 12 h to remove any water content. The ground powders were heated twice in air at 1250 °C for 30 h with intermediate grinding and slowly cooled to room temperature.

For the fluorination reaction, the $La_{1-x}Sr_xFeO_{3-d}$ compounds were mixed with a 10% excess of poly(vinylidenefluoride), PVDF (Sigma Aldrich). After thoroughly grinding, the mixtures were slowly heated to 400 °C for 24 h. We would like to make the reader aware that a synthesis temperature of 673 °C was erroneously reported in a former article by Clemens et al. [24], and the actual temperature was 400 °C (673 K).

The success of fluorination was confirmed by comparing the lattice parameters of the as- prepared samples to those reported in [24] (lattice parameters are significantly different between fluorinated and unfluoridated compounds, and both systems, $La_{1-x}Sr_xFeO_{3-d}$ and $La_{1-x}Sr_xFeO_{3-x}F_x$ have been extensively studied and compared to each other in [24]). In [24] (and also in [20], where we would like to refer the reader for more information about proof of composition), Clemens et al. additionally used decomposition reactions and quantification of the decomposition products to confirm the composition of the fluorinated compounds (e.g. 42 $SrFeO_2F \rightarrow 21$ $SrF_2 + 5$ $Sr_4Fe_6O_{13} + SrFe_{12}O_{19}$). In addition, O/F are indistinguishable by means of XRD and NPD experiments, but full occupancy of the anion sites was verified from the NPD diffraction data.

2.2. Diffraction experiments

X-ray powder diffraction (XRD) patterns were recorded on a Bruker D8 diffractometer with Bragg–Brentano geometry and a fine focus X-ray tube with Cu anode. A primary beam monochromator was attached. A LYNX eye detector and fixed divergence slit were used. The total scan time was 16 h for the angular range between 5 and 140° 2θ.

Time of flight neutron powder diffraction (NPD) data were recorded on the high resolution diffractometer (HRPD) at the ISIS pulsed spallation source (Rutherford Appleton Laboratory, UK). 4g of powdered $SrFeO_2F$, $La_{0.2}Sr_{0.8}FeO_{2.2}F_{0.8}$, $La_{0.5}Sr_{0.5}FeO_{2.5}F_{0.5}$ and $La_{0.8}Sr_{0.2}FeO_{2.8}F_{0.2}$ were loaded into 8 mm diameter thin-walled, cylindrical vanadium sample cans and data collected at ambient temperature for 75 μA h proton beam current to the ISIS target (corresponding to ~2 h beamtime) for each sample. Furthermore, $La_{0.5}Sr_{0.5}FeO_{2.5}F_{0.5}$ was also measured at 200, 300 and 400 °C to determine its magnetic ordering temperature.

Structure refinements using both the XRD and NPD data were performed using the Rietveld method with the program TOPAS 4.2 (Bruker AXS, Karlsruhe, Germany) [32]. For the room temperature XRD data the whole 2θ-range was used, while for the NPD data only those data collected in the highest resolution backscattering detector bank (bank 1, average $2\theta = 168.329°$, d_{max} ~2.5 Å) were used. The instrumental intensity distribution for the X-ray data was determined empirically from a sort of fundamental parameters set [33], using a reference scan of LaB_6, and the microstructural parameters were refined to adjust the peak shapes for the XRD data. For the neutron diffraction data, a corresponding TOF shape model was used. Lattice parameters were allowed to be slightly different for neutron- and XRD-data (Δ ~0.01–0.02%), but relative axis lengths were constrained to be the same for both data sets (i.e. $a_{NPD}/b_{NPD} = a_{xRD}/b_{xRD}$) and NPD lattice parameters are given throughout the article. The same positional parameters were used and refined for both data sets. Independent thermal displacement parameters were refined for each type of atom, but those for O and F, and Sr and La, were constrained to the same value. While these parameters were also constrained to be the same both for X-ray- and neutron-powder diffraction data, an additional B overall value was refined for the XRD data accounting for further effects such as absorption or surface roughness. Reflections that showed a large magnetic scattering contribution were omitted from the initial crystallographic refinement. For $La_{0.5}Sr_{0.5}FeO_{2.5}F_{0.5}$, an unusual asymmetry to lower *d*-spacings was found, which was not observed in the XRD pattern and could be related to a partial aging/water uptake of the sample, which we had not observed in fluorinated compounds before. To describe the peak shape appropriately, two further fractions (11.4 and 7.2% of total scattered intensity) of this phase with slightly smaller lattice parameters ($(a/b/c)_{fraction\_1,2} = c_{1,2} \times (a,b,c)_{main\_fraction}$; c_1 and $c_2 = 0.9967$ and 0.9940) were used to better describe the peak shape. However, the lattice parameters of the main phase (81.4% of total intensity) were still in excellent agreement with those found by XRD.

Refinements of the magnetic structures of $SrFeO_2F$, $La_{0.2}Sr_{0.8}FeO_{2.2}F_{0.8}$, $La_{0.5}Sr_{0.5}FeO_{2.5}F_{0.5}$ and $La_{0.8}Sr_{0.2}FeO_{2.8}F_{0.2}$ were performed with the program GSAS [34,35] using the NPD data collected from all of the HRPD detector banks. Unit cell, atomic position and atomic displacement parameters were set to the refined values from the previous coupled analysis of NPD- and XRD-data determined above. A second phase in space group *P*1 with the same lattice parameters that contained only the Fe^{3+}

ions, and for which only the magnetic scattering was calculated was introduced into the refinement. Different orientations of the magnetic moments were then examined.

2.3. Magnetic measurements

DC susceptibility measurements were performed over the temperature range 5–300 K using a Quantum Design MPMS SQUID magnetometer. The samples were pre-cooled to 5 K in zero field (ZFC) and also in an applied field of 0.05 T (FC) and values of χ measured whilst warming in a field of 0.05 T. Field-dependent DC susceptibility measurements were performed on the same instrument at 5 K between 0 and 5 T.

3. Results and discussion

3.1. Mode analysis of recently published data

Using the program AMPLIMODES [36] we first performed a symmetry mode analysis of the *Pnma* structures reported in [24], which were determined from XRD data. The analysis was limited in each case to the distortion of displacive type, i.e. that produced by relative atomic displacements considering the disordered mixed O/F sites as a single atomic species. An analysis of this type permits for each composition to decompose the observed structural displacive distortion (with respect to the cubic perovskite) into different contributions that are in general caused by different mechanisms.

The application of group theoretical methods to the description of structural distortions and phase diagrams dates back to Landau and its theory of phase transitions [37]. The structural distortion is decomposed into distortion modes that transform according to different irreducible representations (irreps) of the parent space group. Distortion modes corresponding to different irreps are necessarily uncoupled in the lowest approximation, as mixed quadratic terms are forced by symmetry to be zero [38]. In principle, the parameterization of the distortions in terms of symmetry adapted modes can resolve and separate the specific atomic displacements which are stabilizing the observed phase (primary modes), from those that appear by some high-order coupling and have a secondary marginal role. Thus, the degrees of freedom of the distorted structure expressed in this form have in most cases a clear hierarchy, and subtle changes that may take place with temperature or composition can be better monitored and characterized. In particular, the specific distortions associated with the order parameter(s) of the investigated phase can be identified and quantified. Computer programs are freely available for this type of studies [36,39]. The most recent one, AMPLIMODES [36] has introduced a novel parameterization of the mode decomposition, by defining an amplitude for each irrep mode, together with a polarization vector subject to a normalization with respect to a chosen reference parent structure. This is the parameterization used here. The irrep distortion modes present in the investigated structure are classified according to an irrep of the parent space group, and their symmetry properties are specified by a modulation wave vector (*k*-vector), an irrep label (the irrep labels used here follow the standard of [39]) and a so-called isotropy subgroup, which is the symmetry (a subgroup of the parent space group) maintained by this specific irrep mode. The atomic displacements associated with a given irrep distortion mode are then defined by a normalized polarization vector describing the relative atomic displacements involved, and a global amplitude. A recent review of the state of the art of this type of mode analysis and its applications can be found in [31].

Table 1
Summary of the symmetry mode decomposition of the *Pnma* structures of $La_{1-x}Sr_xFeO_{3-x}F_x$ reported in [24]. Only three representative compositions are listed. A parent cubic perovskite with average cell parameter 3.93 Å has been used as a reference structure, with the unit cell origin chosen at the iron site. The analogous mode decomposition of a typical *Pnma* distorted perovskite ($SrZrO_3$) is also listed for comparison. Only the symmetry character of each irrep mode present in the structure and its global amplitude are listed.

***k*-Vector**	**Irrep**	**Isotropy subgroup**	**Amplitudes (Å)**			
			$SrZrO_3$	**$La_{1-x}Sr_xFeO_{3-x}F_x$**		
				***x*=0.1**	***x*=0.5**	***x*=0.8**
(1/2 1/2 1/2)	R^{4+}	*Imma*	1.19	1.18(5)	0.99(2)	0.76(3)
(1/2 1/2 1/2)	R^{5+}	*Imma*	0.07	0.06(3)	0.05(2)	0.22(3)
(0 1/2 0)	X^{5+}	*Cmcm*	0.34	0.316(7)	0.14(5)	0.02(3)
(1/2 1/2 0)	M^{2+}	*P4/mbm*	0.01	0.10(4)	0.10(6)	0.0(7)
(1/2 1/2 0)	M^{3+}	*P4/mbm*	0.79	0.66(4)	0.29(6)	0.0(7)

Table 1 summarizes the results of the mode analysis of the structures reported in [24] for some representative compositions. The table lists the irrep distortions present in the reported structures and their global amplitudes. It also includes for comparison the result for $SrZrO_3$. The amplitudes of the different distortion modes, especially their relative values, are similar in many *Pnma*-distorted perovskites [31], $SrZrO_3$ is taken here as a typical example. One can therefore see in Table 1 that for small *x* the *Pnma* distortion in $La_{1-x}Sr_xFeO_{3-x}F_x$ is similar to that of other *Pnma*-distorted perovskites. The structure is mainly the result of two tilting modes of the oxygen octahedra, with symmetries labeled as R^{4+} and M^{3+} (see Fig. 1), and having as *isotropy subgroups* (invariance symmetries) the space groups *Imma* and *P4/mbm*, respectively. This main feature can be directly derived from the much larger amplitudes of these two modes and the fact that they can explain completely the symmetry break into the *Pnma* space group. The *Pnma* symmetry of the phase is just the intersection of the two symmetry groups that would result from the presence of either one or the other tilting mode separately [31]. These two rigid-unit modes, which are often unstable in the cubic configuration of many perovskite-like structures, act as the driving force for the distorted *Pnma* phase. The remaining distortion modes are secondary degrees of freedom with much smaller amplitudes, which appear due to their compatibility with the symmetry break produced by the two mentioned primary distortions. According to their isotropy subgroup, two of these secondary modes (X^{5+} and M^{2+}) are triggered by the simultaneous presence of both tilting modes, while the mode R^{5+}, as its isotropy subgroup *Imma* coincides with that of the primary tilting R^{4+}, would in principle be allowed in an hypothetical *Imma* phase resulting from the single instability of the R^{4+} mode (for a review of the symmetry mode analysis of these systems see Ref. [31]).

This familiar scenario disappears in Table 1 as *x* increases. It can be seen that for $x=0.5$, the amplitude of the second primary mode M^{3+} is reduced to less than half with respect to $x=0.1$, and for $x=0.8$ it is zero. In fact, at $x=0.8$, only the modes compatible with the higher symmetry *Imma* have significant non-zero amplitudes, with a remarkable increase of the amplitude of the R^{5+} mode, with respect to low *x* compositions. Fig. 2 depicts a more global picture of the variation with *x* of the amplitudes of the different distortion modes in the structures reported in [24]. A clear indication emerges that a change of behaviour takes place about $x=0.6$. As *x* increases in value, the amplitudes of the two primary tilting modes decrease, especially the M^{3+} mode, and the secondary modes either remain marginal with large relative errors, or if they have significant amplitudes as for the X^{5+} distortion, they decrease in accordance with the decrease of the driving tilting

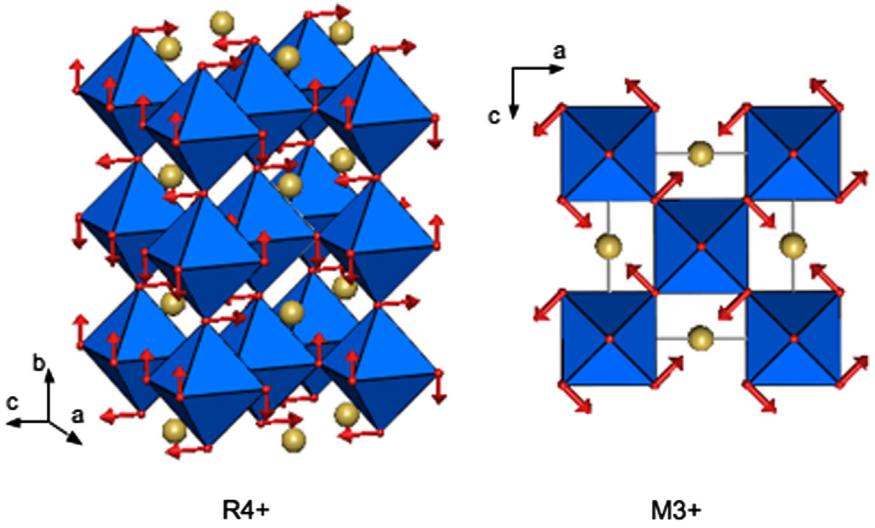

Fig. 1. The two primary distortion modes with respect to the cubic perovskite that are present in *Pnma* perovskites. They represent two tilting schemes of the oxygen octahedra.

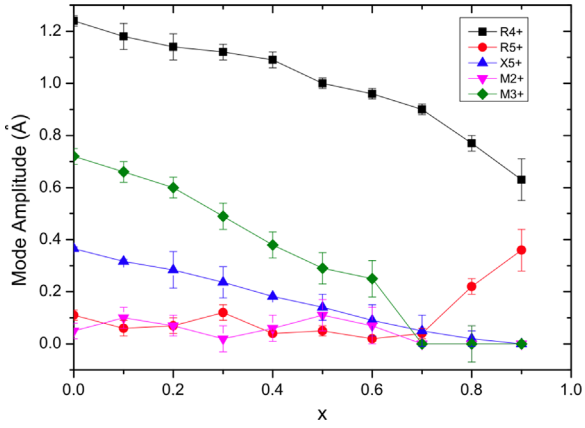

Fig. 2. Amplitudes as a function of x of the distortion modes present in the structures of $La_{1-x}Sr_xFeO_{3-x}F_x$ reported in [24].

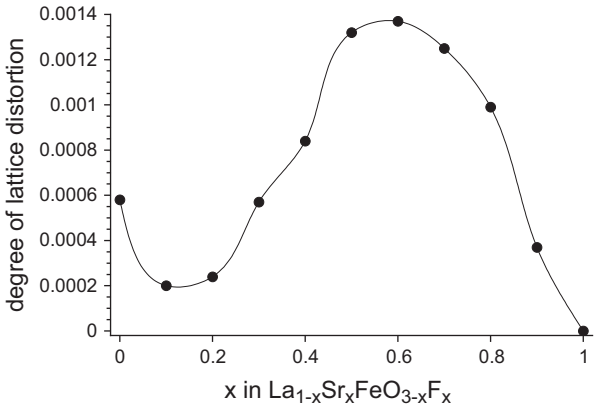

Fig. 3. Degree of lattice distortion as average orthorhombic strain for the lattice parameters of the compounds of the system $La_{1-x}Sr_xFeO_{3-x}F_x$ reported in [24].

modes. For $x \geq 0.7$, however, the tilting mode M^{3+} disappears with only the distortion modes R^{4+} and R^{5+} having non-negligible values, and the amplitude of the R^{5+} mode increases significantly as x increases while the R^{4+} tilting continues decreasing. The effective symmetry for $x \geq 0.7$ is therefore *Imma*. This change in symmetry is also indicated from an analysis of the degree of lattice distortion (calculated from the lattice parameters reported in [24] using the STRAIN program of the Bilbao Crystallographic Server [40–42]), for which a clear change of slope is indicated for $x < 0.7$ (see Fig. 3). The degree of lattice distortion has been calculated with respect to a lattice with the same volume per unit cell but having the ideal cubic metrics, so that it becomes a kind of average orthorhombic strain, namely the square root of the sum of the squared strain tensor components along the three orthorhombic axes divided by 3. It seems therefore that this composition range corresponds to another phase, and the significant weight of the R^{5+} distortion clearly shows that its type is quite different from the usual *Pnma* phase in distorted oxide perovskites. This new phase is not only the result of suppressing the M^{3+} tilting mode, but also the R^{5+} distortion seems to play an important role. It is not acting as a marginal degree of freedom as happens in the *Pnma* phase, but it becomes a significant part of the structural distortion. In this range of high fluorination the R^{5+} distortion mode, which distorts the anion octahedra, behaves as if it were an additional primary order parameter, despite its compatibility with the symmetry break of the R^{4+} tilting. This is evidenced by the fact that its magnitude increases while the tilting mode decreases.

An interesting point to note is that, while the $x=1$ compound $SrFeO_2F$ has been reported from XRD data to be cubic with the ideal perovskite structure [14,15,43], this high symmetry is difficult to reconcile with the mode behaviour shown in Fig. 2. Although the amplitude of the tilting R^{4+} mode, following its decreasing tendency, could indeed become zero at this limit composition, the amplitude of the R^{5+} distortion increases as x approaches 1. This suggests that the $x=1$ compound should also have *Imma* symmetry.

The analysis above thus shows that the phase symmetry for samples with high strontium content is probably higher than *Pnma*. This higher symmetry can be understood in terms of group–subgroup relationships (see Supplementary material) and this has already been discussed in other reports [44] in a similar fashion. The space group *Imma* is a supergroup of *Pnma*. This may explain why the distortions and relaxations of the structure could only be approximately described in our earlier report [24]. The number of degrees of freedom for the refinements might have been too high for some of the compositions and the very small shift of $(O/F)_1$ along the a- and of $(O/F)_2$ along the *a*- and *c*-axis in the structural models reported in [43] for $x \geq 0.5$ should be revised. It therefore seemed appropriate to revisit this system by means of a detailed NPD analysis, reported in the following section, and thus try to

confirm the rather new phase diagram scenario inferred from the symmetry-mode analysis discussed above.

3.2. Structural characterisation of the $La_{1-x}Sr_xFeO_{3-x}F_x$ system

An overview of HRPD bank 1 data recorded for different samples of the system $La_{1-x}Sr_xFeO_{3-x}F_x$ is given in Fig. 4. Comparing the samples $La_{1-x}Sr_xFeO_{3-x}F_x$, the pattern for the compound with $x=0.2$ is different from the ones for $x \geq 0.5$, in that it is richer in reflections. The reflections can be indexed on the basis of a distorted perovskite with space group *Pnma*. The refined structure is reported in Table 2, and the plot of the coupled Rietveld analysis is shown in Fig. 5.

The Fe–$(O/F)_{1,2}$ distances were calculated to be 1.993(2) and 2.003(1) Å. In addition, the angles of the octahedron do not shift much away from the ideal angles of 90° (see Table 3). Therefore, the octahedra can be considered as essentially undistorted. In addition, the metric distortion of the compound is very low and the lengths of the cell axes therefore relate to a pseudocubic length. This can also be seen in the normalized lattice parameters (see Fig. 6), which were calculated according to

$$(a,b,c)_{\text{norm.}} = \frac{(a,b,c)}{k \times \sqrt[3]{V_{f.u.}}}$$

with $k=2$ for b and $k=\sqrt{2}$ for a, c. $V_{f.u.}$ is the volume per $La_{1-x}Sr_xFeO_{3-x}F_x$ unit ($=V/4$). Such normalized lattice parameters are related to the components of the strain tensor. In this construction, the values of $(a,b,c)_{\text{norm.}}$ for $La_{0.8}Sr_{0.2}FeO_{2.8}F_{0.2}$ are very close to the value of 1.

For $x=0.8$, some of the superstructure reflections disappear and the patterns can be indexed in the space group *Imma*.

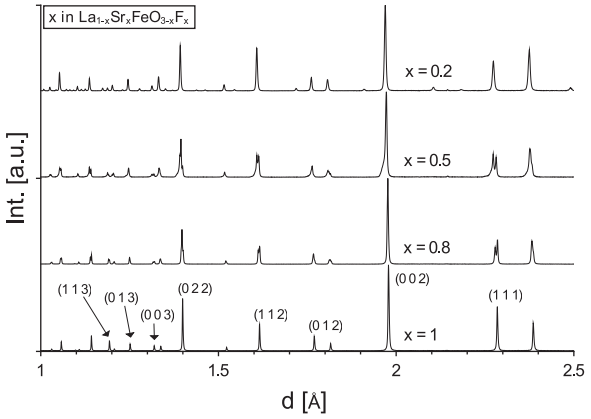

Fig. 4. Neutron powder diffraction patterns of samples in the system $La_{1-x}Sr_x$-$FeO_{3-x}F_x$. *hkl* values are given on the basis of a primitive cubic cell for $SrFeO_2F$ ($x=1$).

For $x=0.5$, superstructure reflections resulting from the loss of the body centering can be found, albeit very broad with a small intensity in the NPD pattern (see Supplementary material). The higher breadth of the peaks might indicate that the domain size of *Pnma* ordering is smaller than the overall domain size and/or only partly expressed. Due to these findings we decided to describe the structure in the lower symmetric space group *Pnma*, but would like to comment that it seems that this sample is on the borderline of the lower symmetry region and we could not entirely rule out the possibility that the symmetry is higher. This is also represented by a further quite small improvement of the fit for a reduced symmetry of *Pnma* instead of *Imma* for the $x=0.5$ phase ($R_{wp}(Pnma)=3.126$ vs. $R_{wp}(Imma)=3.163$; see Fig. 7 for a plot of the Rietveld analysis). Furthermore, the mode analysis reported in Section 3.1 also indicates a reduced symmetry for samples with $x<0.7$. The refined structural data for $La_{0.5}Sr_{0.5}FeO_{2.5}F_{0.5}$ and $La_{0.2}Sr_{0.8}FeO_{2.2}F_{0.8}$ are listed in Tables 4 and 5.

As for the $x=0.2$ sample discussed earlier, the Fe–$(O/F)_{1,2}$ distances are fairly regular for both compounds: 2.0003(4) and 1.9898 (2) Å for $x=0.5$ and 1.9859(4) and 1.9883(3) Å for $x=0.8$. In addition, the bond angles were also found to deviate only slightly from 90° for both compounds (see Table 3), leaving the octahedra essentially undistorted.

Following on from these structure determinations for mixed Sr/La samples, special attention must be drawn to the $SrFeO_2F$ endmember, which was previously reported using X-ray diffraction data to crystallize in the cubic space group *Pm*-3*m* [14,15,20,24]. The neutron diffraction pattern for this compound shows reflections which cannot be indexed on the basis of a primitive cubic cell (see Fig. 4), even at very low *d*-spacings where magnetic scattering can be ruled out due to the rapid decrease of the magnetic form factor for $d \ll 1.5$ Å. This is in agreement with the magnetic structure described later in Section 4.2, which showed that those additional reflections cannot be assigned to magnetic scattering. A detailed structural analysis was therefore performed, and this showed that the pattern could also be indexed on the basis of an orthorhombic perovskite with space group *Imma* as found for samples with $x \geq 0.5$ (see Fig. 8). Remarkably, only a very small deviation (if any at all) of the lattice parameters from a pseudo-cubic cell was observed (see Fig. 6). We therefore tried to refine the patterns by using cubic subgroups of *Pm*-3*m* (such as *Fm*-3*m* and *Fm*-3*c*). However this did not result in a proper description of the peak intensities, attributed to the fact that those subgroups cause a splitting of the A or B site, and a common anion site with one degree of freedom. The underlying symmetry of those cubic subgroups is therefore not suitable to describe the crystal structure, although the pattern could be indexed in principle using these subgroups. It is also worth mentioning that the *Imma* arrangement of the atoms is in very good agreement with what can be expected from the mode analysis of compounds with $x<1$ reported in Section 3.1.

Table 2
Crystal structure of $La_{0.8}Sr_{0.2}FeO_{2.8}F_{0.2}$ (space group *Pnma*) from a coupled Rietveld analysis of HRPD bank 1 NPD and XRD data.

Atom	Wyckoff site	*x*	*y*	*z*	Occupancy	B [Å²]
La^{3+} / Sr^{2+}	$A_1/4c$	−0.0229(2)	**1/4**	0.4953(4)	**0.8** / **0.2**	0.62(1)
Fe^{3+}	$Fe_1/4a$	**0**	**0**	**0**	**1**	0.41(1)
O^{2-} / F^-	$(O/F)_1/4c$	0.0118(4)	**1/4**	−0.0676(6)	**0.9333** / **0.0667**	0.51(1)
O^{2-} / F^-	$(O/F)_2/8d$	0.2227(3)	0.0398(2)	0.2748(3)	**0.9333** / **0.0667**	0.51(1)

***a* [Å]**	5.5608(2)	***b* [Å]**	7.8632(3)	***c* [Å]**	5.5663(2)
R_{wp} [%] (XRD+NPD)	2.67	**GOF (XRD+NPD)**	2.08	**R_{Bragg} [%]**	0.73 (XRD) 11.8 (NPD)

The Fe–$(O/F)_{1/2}$ distances remain quite similar and were determined to be 1.9984(6) and 1.9785(2) Å, respectively. Nevertheless, the shifts of the $(O/F)_1$ and $(O/F)_2$ ions from their ideal cubic positions cause a deviation of $\sim 3^\circ$ of the $(O/F)_1$–Fe-$(O/F)_2$ angle (see Table 3). The refined crystal structure is reported in Table 6. It is also worth mentioning that the mode analysis of the as determined structure of $SrFeO_2F$ (reported later in this section) allowed for the determination of the correct global minimum of the refinement (a local minimum was reached in the initial refinement).

We therefore attempted to determine or rule out possible reasons for this shift of the anions in $SrFeO_2F$. Since the anion site is split into two sites with multiplicities of 4 and 8, ordering of O^{2-} and F^- on the anion sites could be possible. Such ordering was recently observed for the hexagonal perovskites 6H–$BaFeO_2F$ and 15R–$BaFeO_2F$ [19] by a detailed investigation of bond valence sums. However, the bond valence sums for O_1, O_2, F_1 and F_2 were obtained as 1.715, 1.708, 1.423, and 1.418, respectively. Therefore, these differences do not indicate ordering of oxygen and fluorine ions on the anion sites and suggest that the determined position is

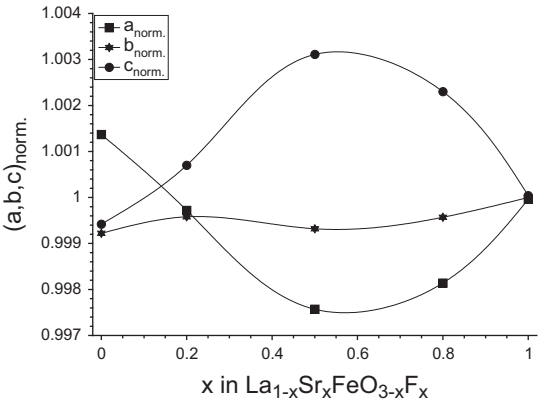

Fig. 6. Dependency of normalized lattice parameters $(a,b,c)/(k \times V_{f.u.}^{1/3})$ ($k=2^{1/2}$ for a and c and $k=2$ for b, taking into account the different lengths of the orthorhombic axes) on the degree of substitution x in $La_{1-x}Sr_xFeO_{3-x}F_x$. For $x=0$, lattice parameters were determined from XRD data only.

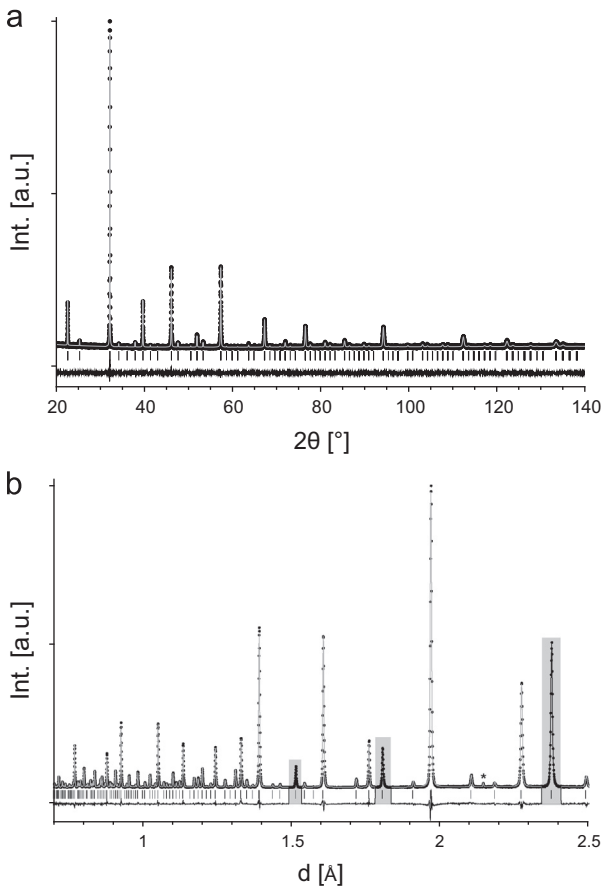

Fig. 5. Coupled Rietveld analysis of XRD (a) and HRPD bank 1 NPD (b) data on the sample of composition $La_{0.8}Sr_{0.2}FeO_{2.8}F_{0.2}$. For the NPD data, reflections that have not been included due to strong contribution of magnetic scattering are marked grey, the reflection from the vanadium sample can is marked with an asterisk.

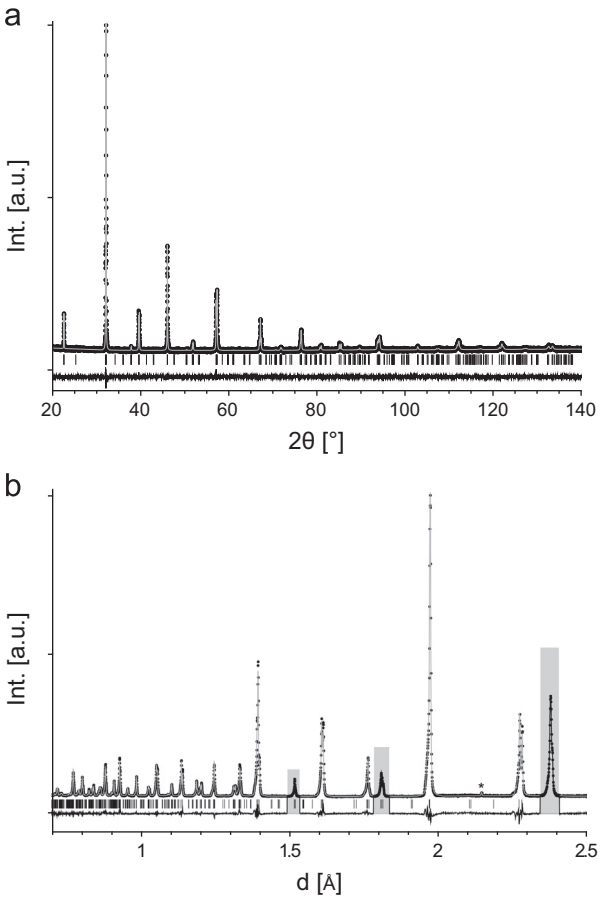

Fig. 7. Coupled Rietveld analysis of XRD (a) and HRPD bank 1 NPD (b) data on the sample of composition $La_{0.5}Sr_{0.5}FeO_{2.5}F_{0.5}$. For the NPD data, reflections that have not been included due to the strong contribution of magnetic scattering are marked grey, the reflection from the vanadium sample can is marked with an asterisk.

Table 3
Selected bond angles for the compounds $La_{1-x}Sr_xFeO_{3-x}F_x$.

(O/F)*x*–Fe–(O/F)*y* angle [°]	**$La_{0.8}Sr_{0.2}FeO_{2.8}F_{0.2}$**		**$La_{0.5}Sr_{0.5}FeO_{2.5}F_{0.5}$**		**$La_{0.2}Sr_{0.8}FeO_{2.2}F_{0.8}$**		**$SrFeO_2F$**	
	$(O/F)_1$	$(O/F)_2$	$(O/F)_1$	$(O/F)_2$	$(O/F)_1$	$(O/F)_2$	$(O/F)_1$	$(O/F)_2$
$(O/F)_1$	180	89.39(5)	180	89.24(4)	180	87.820(1)	180	85.79(1)
$(O/F)_2$	90.61(5)	88.49(7) resp. 91.51(7)	90.76(4)	88.6(1) resp. 91.4(1)	92.180(2)	88.945(1) resp. 91.055(1)	94.21(1)	89.361(2) resp. 90.639(2)

Table 4
Crystal structure of $La_{0.5}Sr_{0.5}FeO_{2.5}F_{0.5}$ (space group *Pnma*) from a coupled Rietveld analysis of HRPD bank 1 NPD and XRD data.

Atom	Wyckoff site	*x*	*y*	*z*	Occupancy	B [Å²]
La^{3+}	$A_1/4c$	−0.0073(5)	**1/4**	0.4975(4)	**0.5**	0.68(2)
Sr^{2+}					**0.5**	
Fe^{3+}	$Fe_1/4a$	**0**	**0**	**0**	**1**	0.68(2)
O^{2-}	$(O/F)_1/4c$	0.0015(12)	**1/4**	-0.0631(4)	**0.8333**	0.92(2)
F^-					**0.1667**	
O^{2-}	$(O/F)_2/8d$	0.2376(5)	0.0346(2)	0.2610(5)	**0.8333**	0.92(2)
F^-					**0.1667**	

***a* [Å]**	5.5575(2)	***b* [Å]**	7.8731(3)	***c* [Å]**	5.5887(2)
R_{wp} [%] (XRD+NPD)	3.13	**GOF (XRD+NPD)**	2.49	**R_{Bragg} [%]**	0.91 (XRD) 4.69 (NPD)

Table 5
Crystal structure of $La_{0.2}Sr_{0.8}FeO_{2.2}F_{0.8}$ (space group *Imma*) from a coupled Rietveld analysis of HRPD bank 1 NPD and XRD data.

Atom	Wyckoff site	*x*	*y*	*z*	Occupancy	B [Å²]
La^{3+}	$A_1/4c$	**0**	**1/4**	0.5002(7)	**0.2**	0.85(2)
Sr^{2+}					**0.8**	
Fe^{3+}	$Fe_1/4a$	**0**	**0**	**0**	**1**	1.13(2)
O^{2-}	$(O/F)_1/4c$	**0**	**1/4**	−0.0408(7)	**0.7333**	1.25(2)
F^-					**0.2667**	
O^{2-}	$(O/F)_2/8d$	**1/4**	0.0302(3)	**1/4**	**0.7333**	1.25(2)
F^-					**0.2667**	

***a* [Å]**	5.5717(3)	***b* [Å]**	7.8908(4)	***c* [Å]**	5.5949(3)
R_{wp} [%] (XRD+NPD)	3.47	**GOF (XRD+NPD)**	2.74	**R_{Bragg} [%]**	2.02 (XRD) 9.84 (NPD)

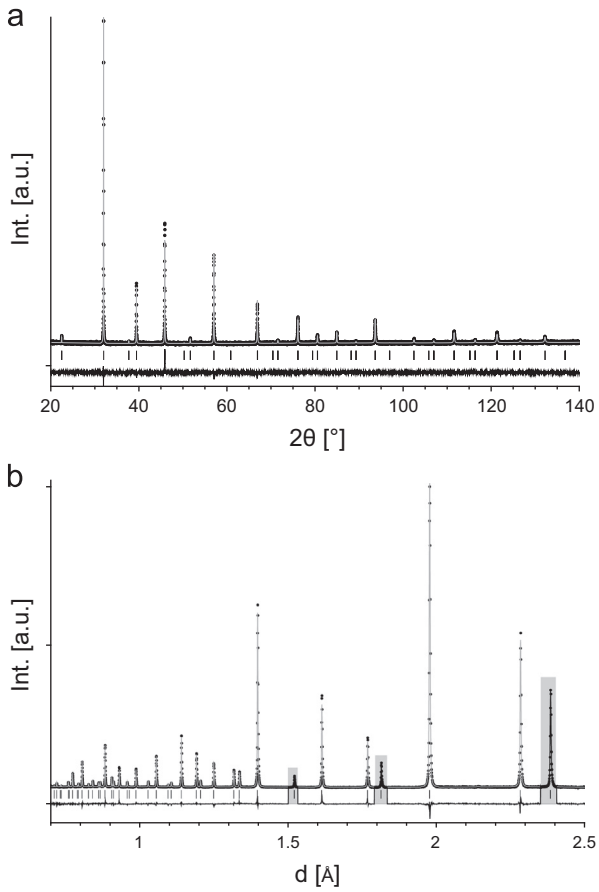

Fig. 8. Coupled Rietveld analysis of XRD (a) and HRPD bank 1 NPD (b) data from the sample of composition $SrFeO_2F$. For the NPD data, reflections that have not been included due to the strong contribution of magnetic scattering are marked grey.

neither ideal for O^{2-} nor for F^- (a similar lack of evidence based on bond valence sums for anion ordering was found for the other compounds of the system). However, as discussed below, mode analysis points to some kind of ordering, and this could also be inferred from a difference Fourier analysis (see Supplementary material), which showed some anomaly around the $(O/F)_1$ position, which could be assigned to F^- from the site multiplicity. In contrast, no such anomaly was found around $(O/F)_2$. The anomaly could be interpreted as altered bonding to Sr^{2+} along the *c*-direction and would be in agreement with a smaller size of F^- compared to O^{2-}. It is also worth mentioning that anion ordering was reported for the compounds $SrTaO_2N$ and $SrNbO_2N$ (O and N can be distinguished by means of neutron diffraction), where the metric distortion remained very low at the same time [45]. However, we have to point out that the metric distortion could also arise from a small size mismatch of the Sr, Fe and O/F ions, which might be indicated by a tolerance factor slightly smaller than one for this compound ($t \sim 0.985$).

The relaxation of the respective ions can also be understood in the following terms. Higher symmetry structures seem to be favoured whenever they are possible. In the Sr rich samples (space group *Imma*), only the $(O/F)_{1,2}$ ions move significantly from their ideal cubic position, hence accounting for the need for neutron diffraction studies to elucidate the lowering of symmetry from cubic for the Sr endmember, $SrFeO_2F$. Due to symmetry, this movement occurs along the *z*- and *y*-directions, respectively. For increasing La content, the lattice parameters of the cell deviate increasingly from the cubic average (see Fig. 6) which was also observed in a previous report [24]. When this metric distortion becomes maximal at $x \sim 0.5$, the symmetry decreases to *Pnma*. By this lowering of symmetry, the metric distortion is decreased, which can be seen by the fact that $(a,b,c)_{norm.}$ become closer to a value of 1. Therefore, the shifts of the $(O/F)_{1,2}$ ions along the *x*- and *x*-/*z*-direction, respectively, and of the (La/Sr) ion along mainly the *x*-direction compensate this metric distortion, making the cell

Table 6
Crystal structure of $SrFeO_2F$ (space group *Imma*) from a coupled Rietveld analysis of HRPD bank 1 NPD and XRD data.

Atom	Wyckoff site	*x*	*y*	*z*	Occupancy	B [Å²]
Sr^{2+}	$Sr_1/4c$	**0**	**1/4**	0.503(1)	**1**	0.95(2)
Fe^{3+}	$Fe_1/4a$	**0**	**0**	**0**	**1**	1.78(2)
O^{2-} F^-	$(O/F)_1/4c$	**0**	**1/4**	−0.016(2)	**0.6667** **0.3333**	1.37(2)
O^{2-} F^-	$(O/F)_2/8d$	**1/4**	0.0264(4)	**1/4**	**0.6667** **0.3333**	1.37(2)

***a* [Å]**	5.5888(4)	***b* [Å]**	7.9043(9)	***c* [Å]**	5.5893(5)
R_{wp} [%] (XRD+NPD)	2.39	**GOF (XRD+NPD)**	1.95	**R_{Bragg} [%]**	2.43 (XRD) 6.60 (NPD)

Table 7
Effective coordination numbers (ECoN) for samples $La_{1-x}Sr_xFeO_{3-x}F_x$.

***x* in $La_{1-x}Sr_xFeO_{3-x}F_x$**	**ECoN**
1	10.4
0.8	10.0
0.5	8.3
0.2	7.6

Table 8
Fe–$(O/F)_{1,2}$–Fe bond angles.

***x* in $La_{1-x}Sr_xFeO_{3-x}F_x$**	**Fe–$(O/F)_1$–Fe [°]**	**Fe–$(O/F)_2$–Fe [°]**
1	174.850(2)	167.925(3)
0.8	166.799(1)	166.251(1)
0.5	159.70(10)	163.41(16)
0.2	158.055(1)	158.499(1)

parameters more similar to those of a cubic cell. Consequently, although the symmetry is lowered from *Imma* to *Pnma* the axis lengths become more similar to each other and we assume that this could be beneficial, for example in terms of lattice energy.

As has already been discussed [24], the effective coordination number (ECoN [30]) decreases for increasing La-content (see Table 7). This can be understood in terms of the ionic radii of the Sr^{2+} and the La^{3+} cations [46]: since Sr^{2+} is larger, and also softer due to its smaller charge than La^{3+}, it is more tolerant to a less strict anion coordination surrounding. Therefore, La^{3+} is likely to optimize its own cation surrounding compared to Sr^{2+} and this can be considered as a main driving force for the change in symmetry.

A further driving force for this distortion lies probably in the "need" to leave the octahedra around Fe^{3+} as undistorted as possible, while relaxing the structure at the same time due to a decrease in Goldschmidt's tolerance factor ($t(SrFeO_2F)=0.985$ vs. $t(LaFeO_3)=0.955$ [24]), and regular coordination polyhedra are considered to be energetically favourable for small highly charged cations. For decreasing symmetry, going from $SrFeO_2F$ to $La_{0.5}Sr_{0.5}FeO_{2.5}F_{0.5}$, the increase of metric distortion causes a decrease in the $(O/F)_1$–Fe–$(O/F)_2$ angle closer to 90°, along with a simultaneous increase in the $(O/F)_2$–Fe–$(O/F)_2$ angle (away from 90°). The change of symmetry from *Imma* to *Pnma* could be beneficial in terms of "not distorting" the octahedra any further, but results in their tilting in other directions. This is also reflected in the bond angles Fe–$(O/F)_{1,2}$–Fe (see Table 8), which express the degree of tilting by the amount of deviation from 180°. For increasing La-content, this tilting increases continuously.

Table 9 summarizes the mode decomposition of the structures, which have been described above, with respect to the ideal cubic perovskite. The data can be compared with those in Table 1. The general features observed in the structural models proposed in

Table 9
Summary of the symmetry mode decomposition of the new *Pnma* and *Imma* structural models of $La_{1-x}Sr_xFeO_{3-x}F_x$ reported in this article. The reference cubic structure is the same as in Table 1.

***k*-Vector**	**Irrep**	**Isotropy subgroup**	**Amplitudes (Å)**			
			***x*=0.2**	***x*=0.5**	***x*=0.8**	***x*=1.0**
(1/2 1/2 1/2)	R^{4+}	*Imma*	1.158(6)	1.032(5)	0.795(7)	0.54(1)
(1/2 1/2 1/2)	R^{5+}	*Imma*	0.108(6)	0.058(2)	0.153(7)	0.29(1)
(0 1/2 0)	X^{5+}	*Cmcm*	0.287(3)	0.075(9)	–	–
(1/2 1/2 0)	M^{2+}	*P4/mbm*	0.027(5)	0.00(1)	–	–
(1/2 1/2 0)	M^{3+}	*P4/mbm*	0.579(5)	0.19(1)	–	–

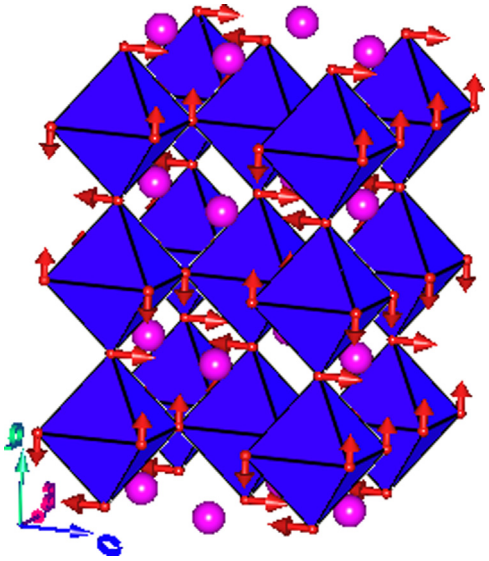

Fig. 9. R^{5+} distortion mode with respect to the cubic perovskite present in the *Imma* phase observed at high values of fluorine substitution/Sr rich samples. It distorts the cation–anion bond angles within the octahedra and its amplitude increases with the degree of fluorination.

[24] are confirmed. Apart from the suppression of the M^{3+} tilting mode at high degrees of fluorination, it is clear that the R^{5+} mode behaves very differently in the *Imma* phase. Its amplitude increases significantly in this phase as the degree of substitution increases, although it does not reach the high values present in the structural models obtained with less experimental accuracy in [24]. The change of behaviour of the R^{5+} mode in the *Imma* phase can be detected not only in its amplitude variation, but also in its internal structure, i.e. its so-called polarization vector [31]. This mode involves in general both displacements of the La/Sr atoms and the oxygen atoms as it combines two basis symmetry modes,

one for the La/Sr and one for the oxygen. In the *Pnma* phase for $x=0.2$ and 0.5, the weight of the La/Sr displacements is quite significant in this linear combination (the two modes combine in an approximate ratio 2/5) for the two compositions, while in the *Imma* phase the R^{5+} mode is essentially restricted to the anions. This mode is shown in Fig. 9, where it can be seen to distort the octahedra (for small amplitudes only the bond angles change). This distortion mode of the octahedra could be the signature of some small ordering of the F/O sites, such that the two independent O/F sites do not have exactly the same F/O occupation ratio, the difference increasing with x. This occupation asymmetry of the octahedral anion sites could be at the origin of the activation of the displacive distortion of the octahedra through the R^{5+} mode.

Table 9 also shows that the mode amplitudes for the limiting composition $x=1$ are fully consistent by continuity with the values for lower compositions, confirming the soundness of an orthorhombic *Imma* model for this phase, in contrast with the cubic configuration that had been considered previously using only X-ray diffraction data.

4. Magnetic characterisation of the system $La_{1-x}Sr_xFeO_{3-x}F_x$

4.1. SQUID measurements

The samples of composition $La_{1-x}Sr_xFeO_{3-x}F_x$ ($x=1.0$, 0.8, 0.5, 0.2, 0.0) were magnetically characterized via field cooled (FC)/zero field cooled (ZFC) measurements. All the samples showed a similar temperature dependence of the FC/ZFC curves (shown for $SrFeO_2F$ and $La_{0.5}Sr_{0.5}FeO_{2.5}F_{0.5}$ in Fig. 10). The magnitudes of χ indicated antiferromagnetic ordering of the magnetic moments which was confirmed by a detailed investigation of the magnetic structure reported in Section 4.2. Furthermore, the divergence of the FC and the ZFC is indicative of a small canting of the magnetic moments. Unfortunately, the canting angle that would correspond to such a low magnetic moment is too small to be determined by NPD.

Although the shape of the ZFC/FC curves is rather similar, χ for $SrFeO_2F$ ($\sim 3\times10^{-8}$ m³/mol) and for $La_{0.5}Sr_{0.5}FeO_{2.5}F_{0.5}$ ($\sim 3\times10^{-7}$ m³/mol) differ by approximately one order of magnitude. It was observed that the magnitude of χ increases as x changes from 1 to 0.5, then decreases when x decreases further to 0.2, before increasing slightly again when x decreases to 0. Field dependent measurements were therefore recorded at 5 K for $x=1$, 0.8, 0.5, 0.2 and 0.0 to examine this behaviour in more detail (see Fig. 11). These measurements showed that the magnetic moments per Fe atom (Fig. 12) follow the same trend as has been observed for the magnitude of χ.

The dependency of the magnetic moment per Fe atom follows the change of orthorhombic strain as depicted in Fig. 3. We assume that the deviation of the cell lengths might be responsible for a small canting of the magnetic moments which then causes a small remanent magnetization in the samples. Hence, these results demonstrate that small structural distortions can influence the magnetic properties of compounds which on first inspection are very similar.

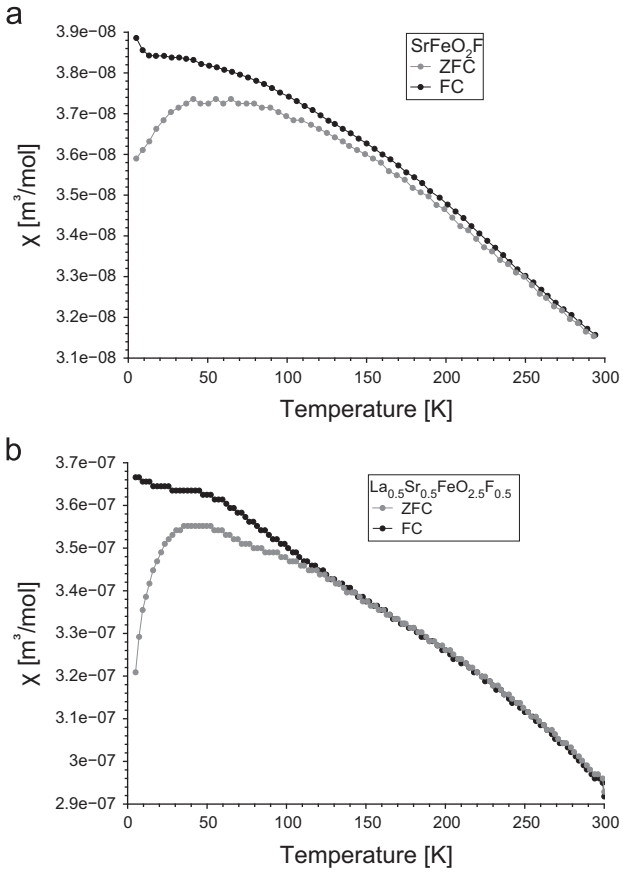

Fig. 10. Field cooled (FC) and zero field cooled (ZFC) measurements of $SrFeO_2F$ (a) and $La_{0.5}Sr_{0.5}FeO_{2.5}F_{0.5}$ (b).

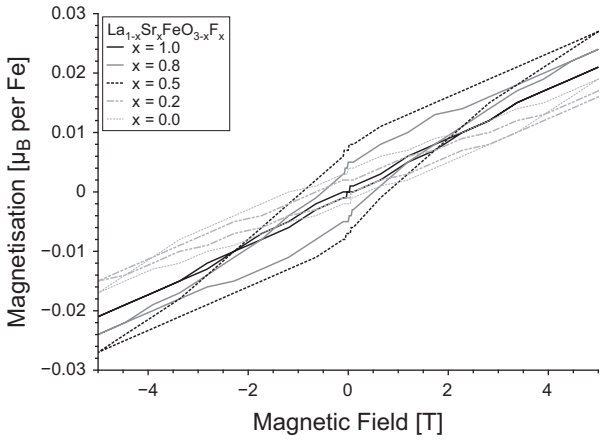

Fig. 11. Field dependent measurements of compounds in the system $La_{1-x}Sr_xFeO_{3-x}F_x$.

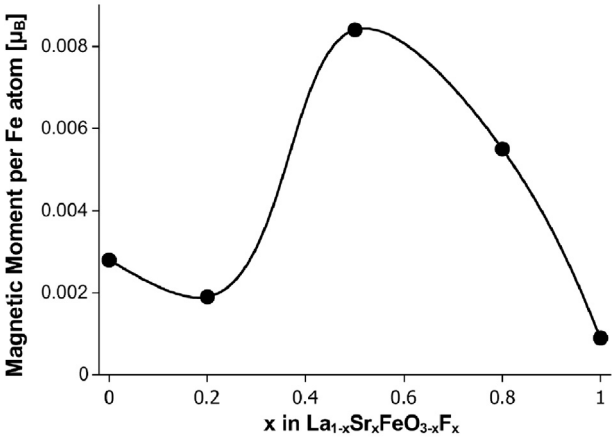

Fig. 12. Magnetic moments per Fe atom for compounds in the system $La_{1-x}Sr_xFeO_{3-x}F_x$.

4.2. Determination of the magnetic structure

Refinements of the magnetic structure were performed using HRPD bank 1, bank 2 and bank 3 data to determine the magnitude and the orientation of the magnetic moments at room temperature (see Fig. 13). All the samples show G-type antiferromagnetic ordering (i.e. the four Fe atoms at positions (0,0,0), (1/2, 0, 1/2), (0, 1/2, 0), and (1/2, 1/2, 1/2) have the signs of their magnetic moments along the prevailing direction correlated in the form (+1 −1 −1 +1). The magnetic moments per Fe atom were determined to lie between 3.36(1) and 3.72(1) μ_B for all the samples ($x=1$, 0.8, 0.5, 0.2). The magnetic moments are therefore similar to other oxyfluoride compounds such as cubic $BaFeO_2F$ [17], 6H-$BaFeO_2F$ [18] and 15R–$BaFeO_2F$ [19]. The deviation from the expected 5.9 μ_B for a high-spin d^5 cation results from the fact that the magnetic moment from NPD is given as $\mu_S+\mu_L-\mu_{covalent}$.

For the determination of the orientation of the magnetic moments, it is necessary that the cell possesses some degree of metric distortion [47]; therefore, such an analysis could only be performed for $La_{0.5}Sr_{0.5}FeO_{2.5}F_{0.5}$ and $La_{0.2}Sr_{0.8}FeO_{2.2}F_{0.8}$. For both samples, the best fit was obtained for an alignment of the magnetic moments along the *c*-axis (see Fig. 14 for a depiction of the crystallographic and magnetic structure of $La_{0.5}Sr_{0.5}FeO_{2.5}F_{0.5}$; for a comparison of the fits of magnetic reflections for $La_{0.5}Sr_{0.5}FeO_{2.5}F_{0.5}$ for the high resolution HRPD bank 1 data see Fig. 15). An orientation of the magnetic moments along the *c*-axis has also been reported for the non F containing endmember $LaFeO_3$ [7,8] and the oxide fluoride compounds with space group *Pnma*/*Imma* reported here are therefore similar to this phase. A G-type ordering of the Fe atoms implies that the Shubnikov space group of this magnetic phase is *Pn′ma′* [48]. This magnetic symmetry also allows A and F-type moment components along the *x* and *y* directions [49], respectively. The observed weak F component must therefore point along the *y* direction.

In order to estimate the Néel temperature of the compounds, a temperature dependent NPD measurement was recorded for $La_{0.5}Sr_{0.5}FeO_{2.5}F_{0.5}$ (see Fig. 16b). Refinement of the magnetic moments on the Fe atoms showed a decrease of the magnetic moment (see Fig. 16a) which allows an estimation of the Néel temperature to be between 300 and 400 °C. Therefore, the compounds of the system $La_{1-x}SrFeO_{3-x}F_x$ show very robust antiferromagnetic ordering. This robustness is related to the presence of iron as single valent Fe^{3+}, which was also found for many similar compounds [28]. In contrast the precursor oxides

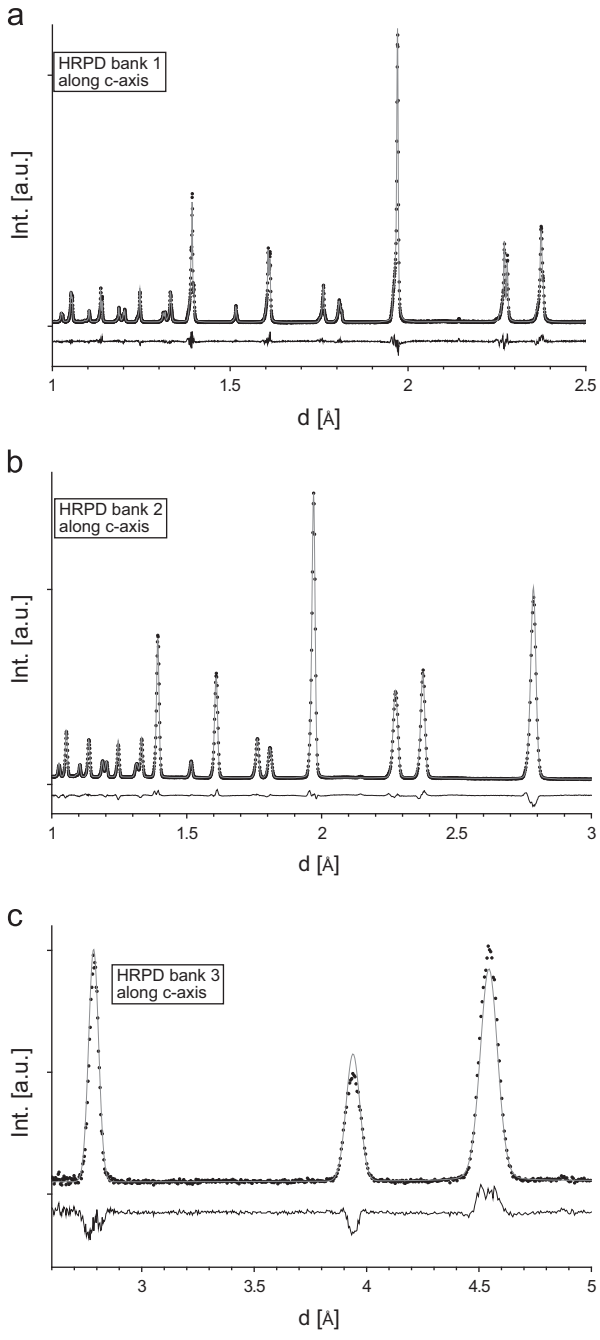

Fig. 13. Rietveld analysis of the magnetic structure of $La_{0.5}Sr_{0.5}FeO_{2.5}F_{0.5}$ HRPD data. Bank 1 (a), bank 2 (b) and bank (3) were simultaneously refined.

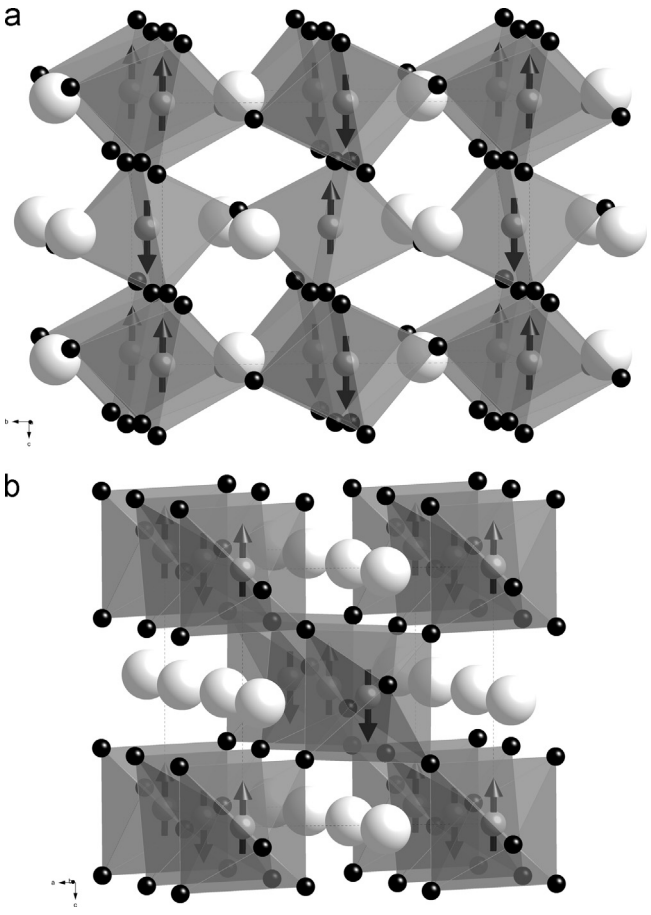

Fig. 14. Crystallographic and magnetic structure of $La_{0.5}Sr_{0.5}FeO_{2.5}F_{0.5}$. Viewing directions are slightly tilted along the *a*- (a) and *b*-axis (b).

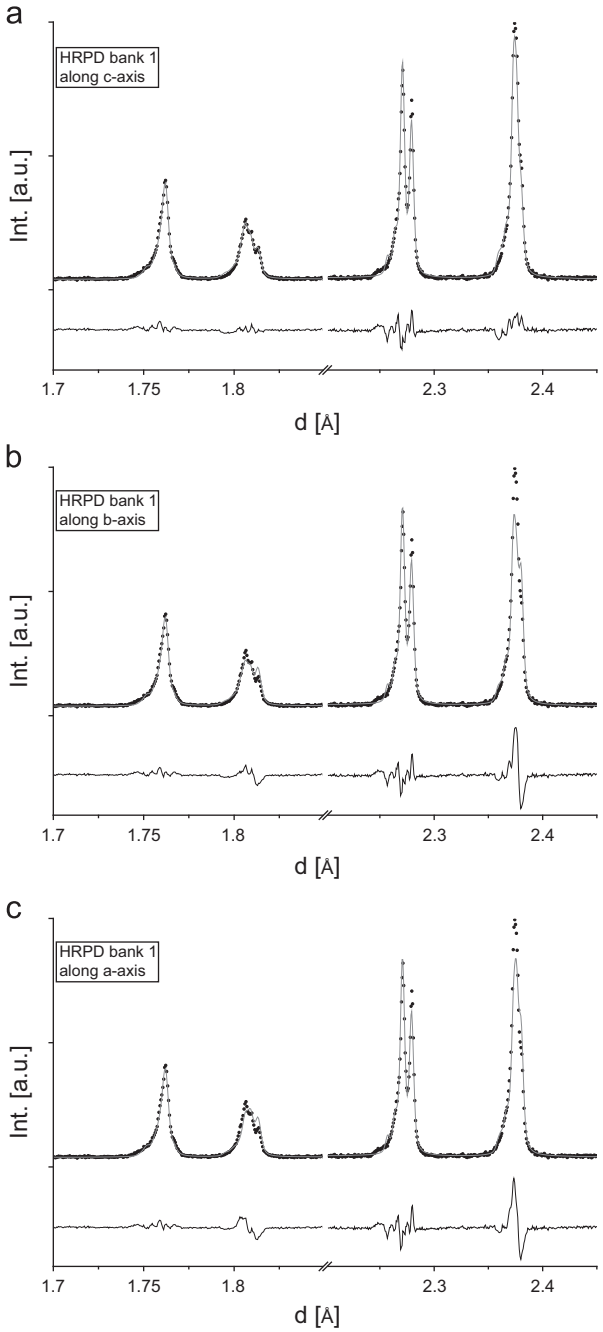

Fig. 15. Comparison of different models for the orientation of the magnetic moment in $La_{0.5}Sr_{0.5}FeO_{2.5}F_{0.5}$. The reflections at 1.75 and 2.27 Å are only influenced by nuclear scattering and therefore not influenced by a change of the direction of the magnetic moments.

$La_{1-x}Sr_xFeO_{3-d}$ show magnetic ordering at room temperature only for La rich compounds ($x \leq 0.3$) [50], i.e. samples that contain high amounts of Fe^{3+}. Hence, fluorination of perovskite compounds can be used to elevate the magnetic ordering temperature of such phases by a change in the average iron oxidation state.

5. Conclusions

Through a study of the series, $La_{1-x}Sr_xFeO_{3-x}F_x$, it has been shown that the description of the structures in terms of symmetry-adapted distortion modes is a helpful means to observe and quantify some trends and common structural properties,

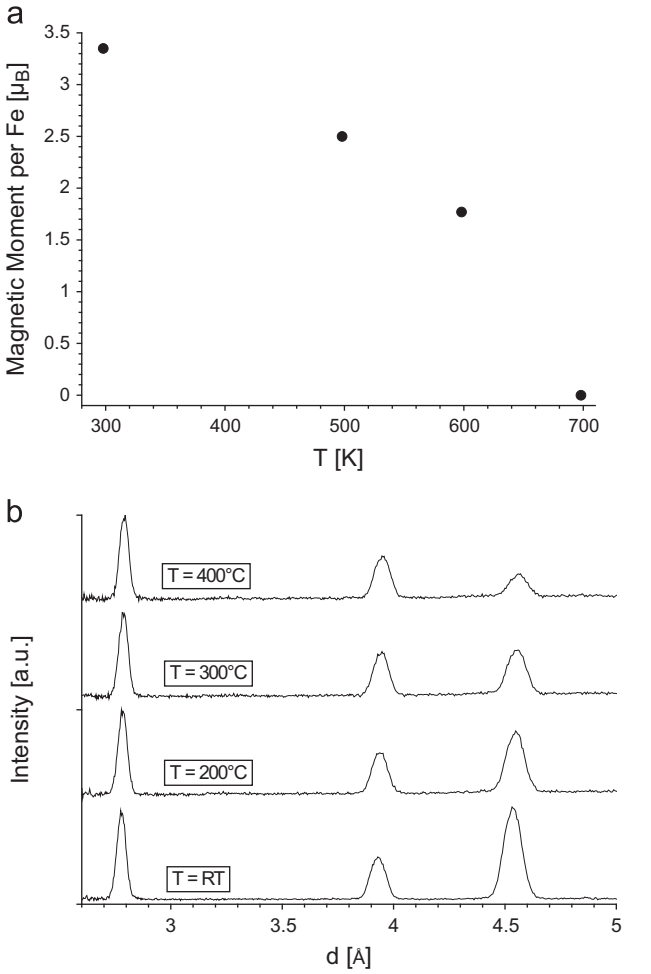

Fig. 16. (a) Temperature dependence of the magnetic moment (b) temperature dependent HRPD bank 2 NPD data recorded on $La_{0.5}Sr_{0.5}FeO_{2.5}F_{0.5}$.

which are difficult to detect from inspection of the atomic positional parameters or the atomic distances of the different structures. For higher fluorine contents (Sr richer samples), including the limit $x=1$, a different phase of *Imma* symmetry has been identified and characterized. This corrects previous reports on the structural properties of this system. In this new phase, a distortion of the octahedra that increases with the degree of fluorination is activated.

The comparison of the mode decomposition of the structures refined for different compositions ensures the consistency of the models with respect to the expected continuity of the amplitudes of the different distortion modes and the invariance of their internal form. This consistency check has allowed us in some cases to avoid false refinement minima which correspond typically to configurations with opposite sign for some secondary mode.

Furthermore, the fluorinated compounds, $La_{1-x}Sr_xFeO_{3-x}F_x$, were shown to be antiferromagnetically ordered at ambient temperatures, with a Néel temperature of ~300–400 °C. Magnetic moments were shown to align parallel to the *c*-axis. FC-ZFC measurements indicate a small canting of the magnetic momets, resulting in a ferromagnetic component with a maximum for $La_{0.5}Sr_{0.5}FeO_{2.5}F_{0.5}$.

Acknowledgments

Oliver Clemens thanks the German Academic Exchange Service (DAAD) for being given a Postdoctoral Research Fellowship.

The Bruker D8 diffractometer used in this research was obtained through the Science City Advanced Materials project: Creating and Characterising Next Generation Advanced Materials, with support from Advantage West Midlands (AWM) and part funded by the European Regional Development Fund (ERDF). Neutron diffraction beamtime at ISIS was provided by the Science and Technology Facilities Council (STFC).

Appendix A. Supporting information

Supplementary data associated with this article can be found in the online version at http://dx.doi.org/10.1016/j.jssc.2013.08.013.

References

[1] J. Mizusaki, M. Yoshihiro, S. Yamauchi, K. Fueki, J. Solid State Chem. 58 (1985) 257–266.
[2] G. Deng, Y. Chen, M. Tao, C. Wu, X. Shen, H. Yang, Electrochim. Acta 54 (2009) 3910–3914.
[3] D. Bayraktar, S. Diethelm, T. Graule, J. Van herle, P. Holtappels, J. Electroceram. 22 (2009). (55-60-60).
[4] H.J. Wei, Y. Cao, W.J. Ji, C.T. Au, Catal. Commun. 9 (2008) 2509–2514.
[5] L. Nalbandian, A. Evdou, V. Zaspalis, Int. J. Hydrogen Energy 34 (2009) 7162–7172.
[6] P.A. Murade, V.S. Sangawar, G.N. Chaudhari, V.D. Kapse, A.U. Bajpeyee, Curr. Appl. Phys. 11 (2011) 451–456.
[7] R.L. White, J. Appl. Phys. 40 (1969) 1061–1069.
[8] J. Lüning, F. Nolting, A. Scholl, H. Ohldag, J.W. Seo, J. Fompeyrine, J.P. Locquet, J. Stöhr, Phys. Rev. B: Condens. Matter 67 (2003) 214433.
[9] P.D. Battle, T.C. Gibb, P. Lightfoot, J. Solid State Chem. 84 (1990) 271–279.
[10] C. Greaves, M.G. Francesconi, Curr. Opin. Solid State Mater. Sci. 3 (1998) 132–136.
[11] E.E. McCabe, C. Greaves, J. Fluorine Chem. 128 (2007).
[12] O. Clemens, P.R. Slater, Rev. Inorg. Chem. http://dx.doi.org/10.1515/revic-2013-0002 (2013).
[13] P.R. Slater, J. Fluorine Chem. 117 (2002) 43–45.
[14] F.J. Berry, X. Ren, R. Heap, P. Slater, M.F. Thomas, Solid State Commun. 134 (2005) 621–624.
[15] F.J. Berry, R. Heap, Ö. Helgason, E.A. Moore, S. Shim, P.R. Slater, M.F. Thomas J. Phys. Condens. Matter 20 (2008) 215207.
[16] R. Heap, P.R. Slater, F.J. Berry, O. Helgason, A.J. Wright, Solid State Commun. 141 (2007) 467–470.
[17] F.J. Berry, F.C. Coomer, C. Hancock, Ö. Helgason, E.A. Moore, P.R. Slater A.J. Wright, M.F. Thomas, J. Solid State Chem. 184 (2011) 1361–1366.
[18] O. Clemens, A.J. Wright, F.J. Berry, R.I. Smith, P.R. Slater, J. Solid State Chem. 198 (2013) 262–269.
[19] O. Clemens, F.J. Berry, J. Bauer, A.J. Wright, K.S. Knight, P.R. Slater, J. Solid State Chem. 203 (2013) 218–226.
[20] O. Clemens, R. Haberkorn, P.R. Slater, H.P. Beck, Solid State Sci. 12 (2010) 1455–1463.
[21] F.J. Berry, X. Ren, R. Heap, P. Slater, M.F. Thomas, J. Phys. Chem. Solids 69 (2008) 2032–2036.
[22] H. El Shinawi, J.F. Marco, F.J. Berry, C. Greaves, J. Mater. Chem. 20 (2010) 3253–3259.
[23] F.J. Berry, A.F. Bowfield, F.C. Coomer, S.D. Jackson, E.A. Moore, P.R. Slater, M. F. Thomas, A.J. Wright, X. Ren, J. Phys. Condens. Matter 21 (2009) 256001.
[24] O. Clemens, M. Kuhn, R. Haberkorn, J. Solid State Chem. 184 (2011) 2870–2876.
[25] F. Iga, Y. Nishihara, T. Katayama, K. Murata, Y. Takeda, J. Magn. Magn. Mater. 104–107 (Part 3) (1992) 1973–1975.
[26] F. Iga, Y. Nishihara, G. Kido, Y. Takeda, J. Magn. Magn. Mater 104–107 (1992) 1969–1972.
[27] K. Mori, T. Kamiyama, H. Kobayashi, T. Otomo, K. Nishiyama, M. Sugiyama, K. Itoh, T. Fukunaga, S. Ikeda, J. Appl. Crystallogr. 40 (2007) s501–s505.
[28] M. Sturza, H. Kabbour, S. Daviero-Minaud, D. Filimonov, K. Pokholok, N. Tiercelin, F. Porcher, L. Aldon, O. Mentre, J. Am. Chem. Soc. 133 (2011) 10901–10909.
[29] T. Peterlin-Neumaier, E. Steichele, J. Magn. Magn. Mater. 59 (1986) 351–356.
[30] R. Hoppe, Z. Kristallogr. 150 (1979) 23–52.
[31] J.M. Perez-Mato, D. Orobengoa, M.I. Aroyo, Acta Crystallogr., Sect. A: Found. Crystallogr. 66 (2010) 558–590.
[32] Topas V4.2, General profile and structure analysis software for powder diffraction data, User's Manual. Bruker AXS, Karlsruhe, 2008.
[33] R.W. Cheary, A.A. Coelho, J.P. Cline, J. Res. Nat. Inst. Stand. Technol. 109 (2004) 1–25.
[34] A.C. Larson, R.B. Von Dreele, Los Alamos National Laboratory Report LAUR (1994) 86-748.
[35] B.H. Toby, J. Appl. Crystallogr. 34 (2001) 210–213.
[36] D. Orobengoa, C. Capillas, M.I. Aroyo, J.M. Perez-Mato, J. Appl. Crystallogr. 42 (2009) 820–833.
[37] L.D. Landau, E.M. Lifshitz, Statistical Physics, Pergamon Press, Oxford, 1969.
[38] H.T. Stokes, D.M. Hatch, J.D. Wells, Phys. Rev. B: Condens. Matter 43 (1991) 11010–11018.
[39] B.J. Campbell, H.T. Stokes, D.E. Tanner, D.M. Hatch, J. Appl. Crystallogr. 39 (2006) 607–614.
[40] M.I. Aroyo, A. Kirov, C. Capillas, J.M. Perez-Mato, H. Wondratschek, Acta Crystallogr., Sect. A: Found. Crystallogr. 62 (2006) 115–128.
[41] M.I. Aroyo, J.M. Perez-Mato, C. Capillas, E. Kroumova, S. Ivantchev, G. Madariaga, A. Kirov, H. Wondratschek, Z. Kristallogr.: Cryst. Mater. 221 (2006) 15–27.
[42] M.I. Aroyo, J.M. Perez-Mato, D. Orobengoa, E. Tasci, G. de la Flor, A. Kirov, Bulg. Chem. Commun. 43 (2011) 183–197.
[43] O. Clemens, R. Haberkorn, P. Slater, H. Beck, Solid State Sci. 12 (2010) 1455–1463.
[44] P. Woodward, Acta Crystallogr., Sect. B: Struct. Sci. 53 (1997) 32–43.
[45] M. Yang, J. Oró-Solé, J.A. Rodgers, A.B. Jorge, A. Fuertes, J.P. Attfield, Nat. Chem. 3 (2011) 47–52.
[46] R.D. Shannon, Acta Crystallogr., Sect. A: Found. Crystallogr. A32 (1976) 751–767.
[47] E.H. Kisi, C.J. Howard, Applications of Neutron Powder Diffraction, Oxford University Press, New York, 2008.
[48] D.B. Litvin, Magnetic Group Tables http://dx.doi.org/10.1107/9780955360220001 (2011).
[49] S.V. Gallego, E.S. Tasci, G. de la Flor, J.M. Perez-Mato, M.I. Aroyo, J. Appl. Crystallogr. 45 (2012) 1236–1247.
[50] S.E. Dann, D.B. Currie, M.T. Weller, M.F. Thomas, A.D. Al-Rawwas, J. Solid State Chem. 109 (1994) 134–144.